# Sn-based redox cycle mediated microenvironment regulation of Cu sites on poly(ionic liquid) enhance electrocatalytic CO-to-$C_{2+}$ conversion

Yi-Ran Du [a],[1], Xiao-Qiang Li [a],[1], Guo-Yi Duan [a],[*], Yue Pan [a], En-Lai Gao [b], Bao-Hua Xu [a],[*]

[a] Beijing Key Laboratory for Chemical Power Source and Green Catalysis, School of Chemistry and Chemical Engineering, Beijing Institute of Technology, Beijing 100081, China
[b] Department of Engineering Mechanics, Wuhan University, Wuhan, Hubei 430072, China

## ABSTRACT

Electrocatalytic CO reduction provides a sustainable route for high-value CO utilization. To promote the selectivity of $C_{2+}$ products ($FE_{C2+}$) at high reaction rates, the electronic structure and the microenvironment of Cu sites in Cu@PIL were regulated by introducing a Sn-mediated redox cycle. The obtained Cu@PIL@Sn-x hybrids provided high $FE_{C2+}$ (> 70%) within a wide current density ($j$) range from −100 to −700 mA cm$^{-2}$. Particularly, an excellent $FE_{C2+}$ of 96.8 % with a high $j_{C2+}$ of −484.2 mA cm$^{-2}$ was obtained on Cu@PIL@Sn-1.0. Besides, it exhibited high tolerance of diluted CO gas at −250.0 mA cm$^{-2}$. Mechanistic studies demonstrated the rich high-valence Cu species and the adjacent Sn-Cl species at the Cu@PIL@Sn-x hybrids jointly account for the local enrichment of oxygen-containing species on Cu surface during the electrolysis of CO, even at high overpotentials, which enables the C–C coupling at high reaction rates.

## 1. Introduction

Carbon monoxide (CO) is an important raw material in chemical industry [1–3]. Conventional CO conversion processes require high temperature and high pressure. The transformation of CO into highly value-added ($C_{2+}$) chemicals driven by renewable electricity (*i.e.*, CORR) under mild conditions is of great theoretical and practical significance [4–7]. In addition, the electrocatalytic CO-to-$C_{2+}$ conversion also represents the key step of electrocatalytic carbon dioxide reduction (CO$_2$RR) leading to $C_{2+}$ products [8,9]. It's significant to reach an efficient tandem CO$_2$-to-CO-to-$C_{2+}$ conversion by fabricating electrocatalytic CO-to-$C_{2+}$ system with high activity, high stability, and high selectivity [10,11]. To date, it's still challenging to obtain a high selectivity towards $C_{2+}$ products ($FE_{C2+}$ > 95%) at current densities larger than −500 mA cm$^{-2}$ in the field of CORR[11].

The promising route is to promote the selectivity of C–C coupling at large reaction rates. A series of advanced strategies in terms of the catalyst design have been developed accordingly, such as coordination polymer decorated [12,13], halogen modification [14], and morphology control [7]. The particularly efficient strategy is to create high-valence Cu components (*e.g.*, Cu(OH)$_2$ and CuO) [15–18]. The intricate grain boundaries and exposed high-index facets upon the *in-situ* reduction of

high-valence Cu species during the electrolysis were supposed to promote the C–C coupling. Besides, the surficial adsorbed oxygen-containing species (*e.g.*, the adsorbed O atom, *O, and the adsorbed OH, *OH) on the Cu surface could regulate the selectivity to different $C_{2+}$ products [18,19]. Correspondingly, several synthetic methods have been developed to provide Cu-based materials with a high-valence state, including solution oxidation [17,20], thermal annealing [21], heat and quench [15], and electrochemical oxidation [16]. However, the dispersion and exposure of the active sites are insufficient by these methods, which are not conducive to reaching high current density.

Very recently, our group developed poly(ionic liquid)-Cu hybrids (*i.e.*, Cu@PIL), wherein Cu nanoparticles (NPs) were embedded in the PIL matrix with good conductivity in a high-dispersed manner [22,23]. Remarkably, the dense chelating sites and the electrostatic networks of the PIL are beneficial for impregnation of second metal salt [24–26]. Our preliminary analysis indicated the aerobic oxidation of Cu(0) to Cu$_2$O, CuO, and Cu(OH)$_2$ is feasible thermodynamically at normal temperatures and pressures (Table S1) [27]. However, continuous oxidation is kinetically unfavorable due to the resistance of the preformed dense oxide layer to O$_2$ diffusion [28]. In this regard, the introduction of a catalytic aerobic oxidation cycle to the microenvironment of

---

pre-dispersed Cu NPs in the PIL by loading the second metal could deliver high-dispersed high-valence Cu nanostructures. To this end, further thermodynamic analysis of the second metal (Section S1 and Table S2 to S9), including Ag, Au, Zn, In, Bi, Sn, Pb, and Hg, was conducted. It shows that the $SnCl_2/SnCl_4$ redox cycle represents the best candidate to enable the aerobic oxidation of Cu(0) to a high-valence state.

To verify our hypothesis, a small amount of Sn(II) chloride (*i.e.*, $SnCl_2$, 0.5–2.0 mol% to Cu NPs) was introduced to the Cu@PIL bearing chloride as the anion by impregnation under air. As a proof of concept, abundant nanosized high-valence Cu species were *in-situ* formed and dispersed around the Cu NPs in the PIL layer. The obtained Cu@PIL@Sn-x hybrids provided high $C_{2+}$ selectivity (> 70 %) within a wide reaction rate range from −100 mA cm$^{-2}$ to −700 mA cm$^{-2}$. Particularly, an excellent $FE_{C_{2+}}$ of 96.8 % with a high $j_{C_{2+}}$ of −484.2 mA cm$^{-2}$ was obtained on Cu@PIL@Sn-1.0 with 100.0 vol% CO gas. Further, it exhibited high tolerance for low concentrations of CO gas at a high reaction rate of −250.0 mA cm$^{-2}$. Mechanistic experiments confirmed the presence of high local concentrations of surfacial adsorbed OH and adsorbed O on the catalytic surface during the CORR process. Importantly, it's attributed to not only the rich high-valence Cu species at the surface but also the adjacent Sn-Cl species. The locally enriched surfacial adsorbed OH and adsorbed O, which are sufficient even at high overpotentials, support the C–C coupling activity at high reaction rates.

## 2. Experimental

### 2.1. Synthesis of Cu@PIL@Sn-x (x = 0.5, 1.0, and 2.0)

The PIL-based Cu-Sn bimetallic hybrids are prepared *via* two steps: i) modifying Cu NPs by radical copolymerization of IL monomer bearing imidazolium-pyridinium-imidazolium (Im-Py-Im) chelation site and the crosslinking agent of divinylbenzene (DVB) (*i.e.*, prepare Cu@PIL), and ii) wet impregnation of $SnCl_2 \cdot 2H_2O$. The synthesis of Cu@PIL was reported in our previous work [26]. In this work, different dosages of $SnCl_2 \cdot 2H_2O$ were introduced to afford Cu@PIL@Sn-x. Herein, x represents the molar percentage of Sn to Cu, of which 0.5 mol%, 1.0 mol%, and 2.0 mol% were studied. The obtained hybrids were loaded on the carbon paper-based gas diffusion electrode (GDE) by airbrushing. The detailed procedures are provided in the Supplementary Information.

### 2.2. Characterizations

X-ray diffraction (XRD) patterns were obtained from an Ultima IV diffractometer with Cu Kα radiation (Rigaku, Japan). High-resolution transmission electron microscopy (HR-TEM) images were collected from a JEM-2100 transmission electron microscope at an accelerating voltage of 200 kV (JEOL, Japan). Scanning electron microscopy (SEM) images were collected from a JSM-7800 F scanning electron microscope at an accelerating voltage of 5 kV (JEOL, Japan). Brunauer-Emmett-Teller (BET) test and pore diameter distribution analysis were obtained from a BELSORP-max analyzer (ANKERSMID B.V, Netherlands). X-ray photoelectron spectroscopy (XPS) measurements were performed on a VersaProbe III X-ray photoelectron spectrometer (ULVCA-PHI, USA). Gas chromatography (GC) measurements were performed on a 7890 gas chromatography system (Agilent, USA). Raman test was conducted on an inVia Qontor confocal Raman microscope (Renishaw, UK) equipped with a 785 nm laser and a 50× objective. $^1H$ nuclear magnetic resonance (NMR) analyses were conducted with an Ascend 400 MHz nuclear magnetic resonance spectrometer (Bruker, Germany).

### 2.3. CORR experiment

The CORR experiments were conducted in a homemade three-chamber flow cell [26]. GDE loaded with catalyst, Ni foam, and mercuric oxide electrode were used as the working, counter, and reference electrodes, respectively. An FAA-3-PK-130 Fumasep anion exchange membrane was used to separate the catholyte and anolyte chambers. Aqueous KOH solution (1.0 M) was used as the electrolyte. The catholyte and anolyte flow rates were set as 1.0 mL min$^{-1}$ and 10.0 mL min$^{-1}$, respectively. High-purity CO was used as the feed gas with a flow rate of 13.3 mL min$^{-1}$. The flow rate of the feed gas was controlled by a mass flowmeter at the inlet. The flow rate at the outlet was measured by a soap film flowmeter. Galvanostatic electrolysis was conducted for all the CORR experiments. CS150H workstation (CorrTest, China) was used for electrolysis. For the linear sweep voltammetry (LSV) and electrochemical impedance spectroscopy (EIS) test, a 660E workstation (CHI, China) was employed. All the cathodic potentials ($E_{cathodic}$) were obtained by converting measured potential ($E_{ref}$) to RHE with $iR_s$ (85 %) compensations using the Eq. (1):

$$E_{cathodic} = E_{ref} + 0.098(V) + 0.059(V) \times pH - iR_s \times 85\% \quad (1)$$

where $i$ is the average current during the test, and $R_s$ is the solution resistance measured by the EIS test.

### 2.4. Product quantification

Gaseous products during electrolysis were quantified using an online 7890 gas chromatography (GC) system (Agilent, USA). $H_2$ and CO were quantified using a thermal conductivity detector (TCD). $CH_4$, $C_2H_6$, and $C_2H_4$ were quantified using a flame ionization detector (FID). The Faradaic efficiency ($FE_g$) for gaseous products was calculated using the Eq. (2):

$$FE_g = \frac{z \times F \times x_g \times f}{i} \times 100\% \quad (2)$$

where $z$ is the electron transfer number, $F$ is the Faraday constant (96,485 C mol$^{-1}$), $x_g$ is the mole fraction of the product, $f$ is the flow rate at the outlet (L s$^{-1}$), and $i$ is the current (A).

Liquid products were quantified using an Ascend 400 MHz nuclear magnetic resonance (NMR) spectrometer (Bruker, Germany). After electrolysis, 400 μL of catholyte was mixed with 200 μL $D_2O$ containing 25 ppm (m/m) DMSO and 250 ppm (m/m) phenol as internal standards, and the peak area ratio of product and standard were used for quantification. The Faradaic efficiency ($FE_l$) for liquid products was calculated using the Eq. (3):

$$FE_l = \frac{z \times F \times c_l \times V}{Q} \times 100\% \quad (3)$$

where $c_l$ is the measured concentration of liquid product (mol mL$^{-1}$), $V$ is the volume of catholyte (50 mL), and $Q$ is the practical electricity consumed during electrolysis (C).

### 2.5. The in-situ Raman analysis

A custom-made electrochemical Raman flow cell was used for the *in-situ* Raman test. A Graphite rod and a mercuric oxide (in 1 M KOH) electrode were used as the counter and reference electrodes, respectively. A piece of CP loaded with catalyst was the working electrode. An anion exchange membrane (FAA-3-PK-130, Fumasep) was placed between the catholyte and anolyte chambers. Aqueous KOH solution (1 M) was used as the electrolyte with a high flow rate of 50 mL min$^{-1}$ to remove the $H_2$ bubbles on the cathode. $CO_2$ with an inlet flow rate of 35 mL min$^{-1}$ was introduced into the gas chamber at the backside of GP. All electrochemical tests were performed with a CS150H workstation (CorrTest, China). The Raman test was conducted on an inVia Qontor confocal Raman microscope (Renishaw, UK) equipped with a 785 nm laser and a 50 × objective.

## 3. Results and discussion

### 3.1. Structural characterizations

The crystal structures of Cu@PIL@Sn-x (x = 0.5, 1.0, 2.0) hybrids were characterized by X-ray diffraction (XRD) patterns (Fig. 1a). Two strong peaks at the 2θ degree of 43.3° and 50.4° (marked with green circles) were ascribed to the (111) and (200) planes of Cu metal, relating to the metallic core of Cu NPs in these hybrids. The weak patterns assigned to $Cu_2O$ were marked with purple boxes. The intensity of these low valent Cu species (*i.e.*, Cu(0) and Cu(I)) related peaks decreases gradually when the Sn/Cu molar percentage (*i.e.*, x value) increases from 0.5 mol% to 2.0 mol%. Notably, a series of patterns (marked with blue boxes) were identified as the diffraction features of $Cu_2(OH)_3Cl$, suggesting the presence of Cu(II) species. The formation of Cu(II) species was attributed to the introduction of Sn salt since no Cu(II)-related pattern was observed on the pristine Cu@PIL (Fig. 1a) [26]. The intensity of these peaks decreases slightly with increasing the x value from 0.5 mol% to 1.0 mol%, followed by increasing rapidly at 2.0 mol%. Considering the gradual consumption of low valence Cu species with the addition of Sn salt, it signifies thus formed Cu(II) species mainly present in an amorphous form in Cu@PIL@Sn-1.0. Besides, no Sn-chlorides- or Sn-oxides-related patterns were assigned in these hybrids. Meanwhile, these patterns were also absent in the hybrid without preloading Cu NPs

(PIL@Sn: obtained by impregnating $SnCl_2 \cdot 2H_2O$ directly to PIL; Fig. S1). It suggests the Sn species at such a scale tend to disperse in an amorphous form.

Brunauer-Emmett-Teller (BET) analysis (Fig. 1b∼1d) indicates Cu@PIL@Sn-x hybrids have abundant micro-mesoporous structures with high specific areas ($S_{BET}$) [29]. In comparison to those of the pristine Cu@PIL (Fig. S2), both $S_{BET}$ of the micropore and the mesopore of Cu@PIL@Sn-0.5 decrease (55.5 m$^2$ g$^{-1}$ to 46.3 m$^2$ g$^{-1}$ and 51.9 m$^2$ g$^{-1}$ to 35.7 m$^2$ g$^{-1}$, respectively). It signifies the porous structure was partially occupied with the introduction of Sn species and the formation of Cu(II) species. Both $S_{BET}$ of the micropore and the mesopore in Cu@PIL@Sn-1.0 further decrease to 24.1 m$^2$ g$^{-1}$ and 33.7 m$^2$ g$^{-1}$, respectively. Interestingly, a sharp increase in $S_{BET}$ of the micropore (50.0 m$^2$ g$^{-1}$) was identified, while that of the mesopore continued to decay (27.3 m$^2$ g$^{-1}$), for Cu@PIL@Sn-2.0. We supposed the newly formed Cu(II) species are sufficient in this case to stack and interwove, thereby creating more microporous structures. It also accounts for the intense XRD patterns of Cu(II) species of Cu@PIL@Sn-2.0.

The high-resolution transmission electron microscopy (HR-TEM) images (Fig. 1e and f, and Fig. S3) were obtained by taking Cu@PIL@Sn-1.0 as an example. It confirms the presence of serried small NPs (∼5 nm) around the large NPs (15–20 nm) in the PIL layer (Fig. 1e). By identifying the distinct lattice fringes, the metallic Cu, $Cu_2O$, and $Cu_2(OH)_3Cl$ were well distinguished (Fig. 1f). Besides, the energy dispersive X-ray
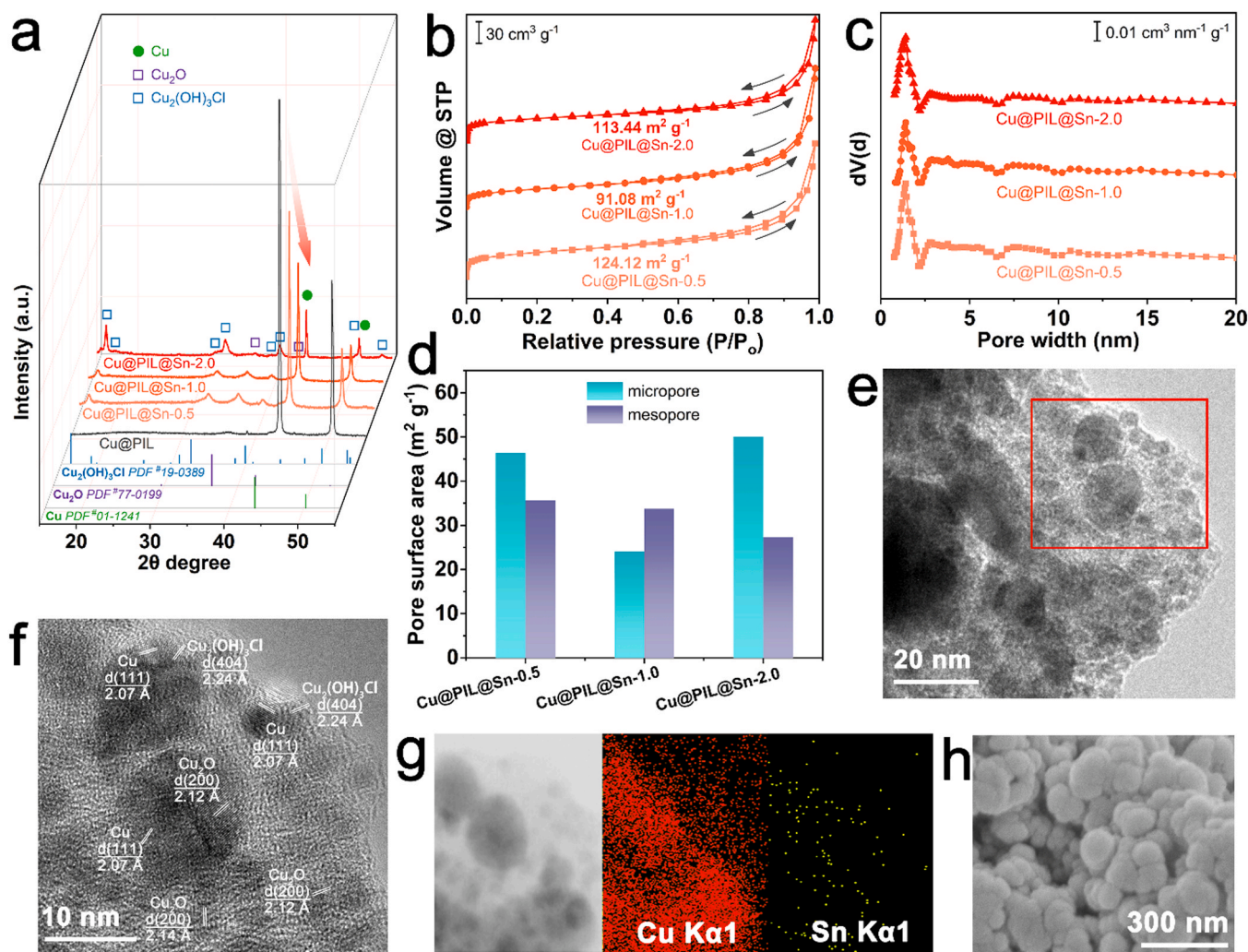


**Fig. 1.** (a) X-ray diffraction (XRD) patterns of Cu@PIL@Sn-x (x = 0.5, 1.0, and 2.0) and Cu@PIL. (b-d) N$_2$ isotherms at 77 K, pore diameter distributions, and pore surface area of Cu@PIL@Sn-x. (e) High-resolution transmission electron microscope (HR-TEM) image of Cu@PIL@Sn-1.0. (f) The enlarged view of the red-box area in (e). (g) Energy dispersive x-ray (EDX) mapping images of Cu@PIL@Sn-1.0. (h) Scanning electron microscope (SEM) image of Cu@PIL@Sn-1.0.

(EDX) images (Fig. 1g) show that both the small and large NPs mainly contain Cu element and bear Sn element sparsely. In this regard, the nano-sized Cu(0), Cu(I), and Cu(II) species exist in a highly fragmented manner, enabling the creation of many Cu(0)-Cu(I), Cu(0)-Cu(II), and Cu(I)-Cu(II) interfaces. Meanwhile, the scanning electron microscopy (SEM) images suggest the Cu@PIL@Sn-x hybrids possess aggregated spherical morphology (Fig. 1h and Fig. S4), which is similar to the pristine Cu@PIL [26].

The chemical environment of Cu elements at the surface of Cu@PIL@Sn-x hybrids was then investigated by a combination of high-resolution X-ray photoelectron spectroscopy (XPS) and Auger spectra (Fig. 2a-b). In Cu $2p_{3/2}$ XPS spectra, the binding energy (BE) of the main peak is close to that of Cu(II) species (*e.g.*, CuCl$_2$/Cu(II) complex at BE of 935.1–935.4 eV [30–32] and Cu(OH)$_2$ at BE of 934.7 eV [33]), while the strong satellite peaks also correspond to the typical features of Cu(II) species [34]. Further analysis by Cu LMM Auger spectra demonstrated that it mainly presents Cu(OH)$_2$, which features the kinetic energy (KE) at 916.8 eV. Besides, a positive shift was observed for the main peak in both XPS and Auger spectra, as the x value increases from 0.5 to 2.0. It's attributed to the variation from Cu(OH)$_2$ to CuCl$_2$ *via* Cu$_2$(OH)$_3$Cl with a higher dosage of Sn salts. In general, the low-valence Cu species at the surface are not high by the XPS and Auger analysis. Particularly, the intensity of Cu(0) featuring at the KE of 918.6 eV [35] is very weak, suggesting the low occupation of metallic Cu. The well-resolved Sn $3d_{5/2}$

peak (Fig. 2c) with the high BE value at ~486.6 eV features the Sn(IV) species [36–39]. It confirms the oxidation of SnCl$_2$ during the preparation of Cu@PIL@Sn-x hybrids. With the addition of SnCl$_2$, the peak intensity increases, which is accompanied with a slightly negative shift of the BE from 486.7 eV to 486.5 eV. It signifies the weak charges transfer (mainly from the Cu species) to the Sn(IV)-species with the increase of Sn(IV) species.

Based on the results of structural characterization and thermodynamic calculations (Section S1 and Table S7) [27], we proposed a tentative route for the *in-situ* formation of high-dispersed high-valence Cu species (Fig. 2d). First, the rich chelating sites, the dense electrostatic networks, and the abundant porous structure of the PIL layer facilitate the introduction of SnCl$_2$ to the vicinity of Cu NPs in a dispersed manner. Second, the aerobic oxidation of metallic Cu(0) and Cu(I) species (*e.g.*, Cu$_2$O) to Cu(II) species (*i.e.*, Cu(OH)$_2$, CuCl$_2$, and Cu(II) chloride hydroxide) occurs along with the redox cycling between SnCl$_2$ and SnCl$_4$ (Section S1 and Table S7). Herein, the hydrolysis of SnCl$_4$ to SnO$_2$ (Table S7) by moisture cannot be completely excluded. In this regard, the Sn(IV) species presenting at the surface might be a mixture of SnCl$_4$ and SnO$_2$, of which the BEs are too close to be distinguished [37–39]. However, the oxidation of low-valence Cu species by SnO$_2$ is thermodynamically unfavorable (Table S7). Thus, the aerobic oxidation continues until the low-valence Cu species near the Sn species are fully converted or the SnCl$_4$ is completely converted to SnO$_2$. Third, the *in-situ*
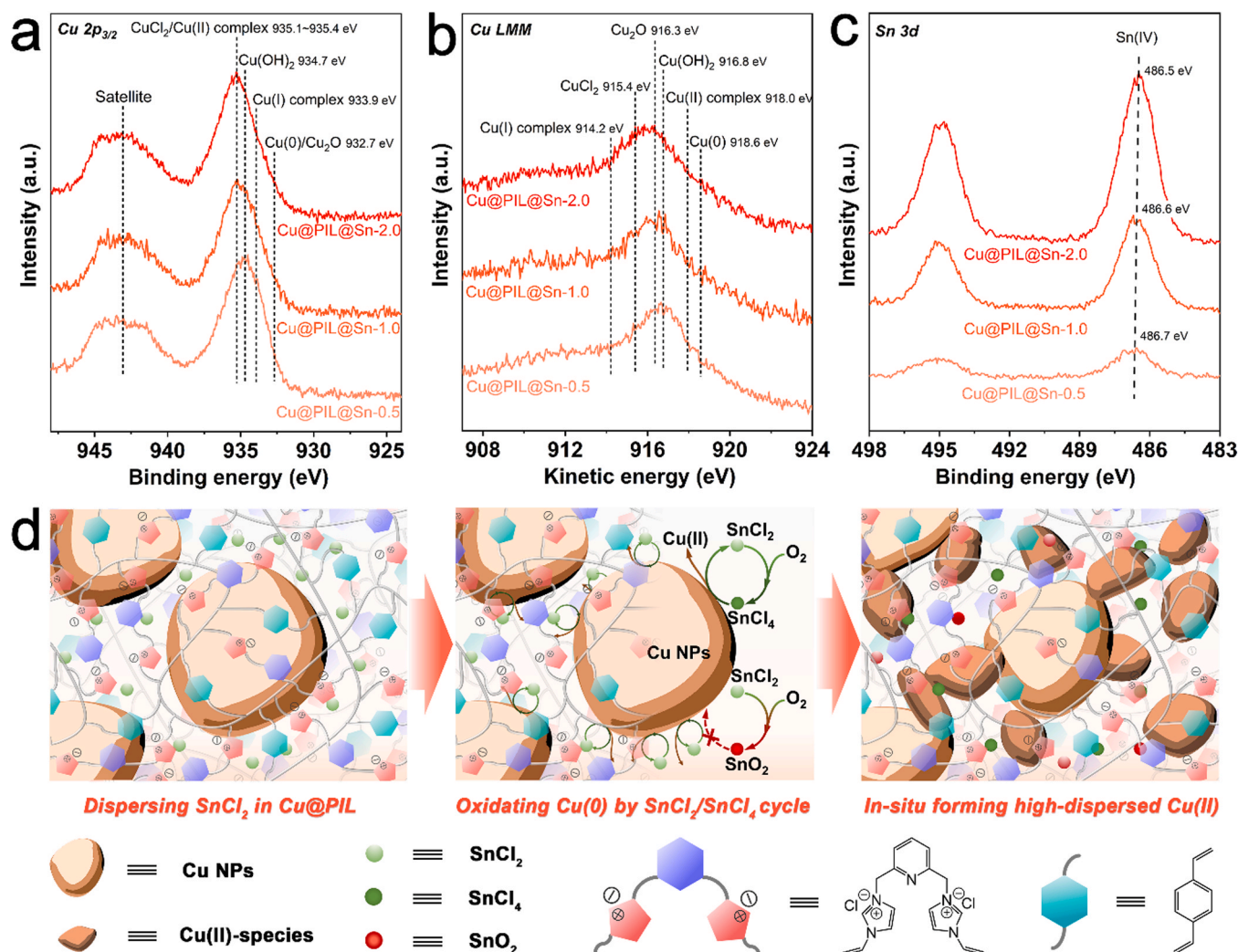


**Fig. 2.** (a-c) X-ray photoelectron spectroscopy (XPS) spectra in Cu $2p_{3/2}$ region, Auger spectra in Cu LMM region, and XPS spectra in Sn 3d region of Cu@PIL@Sn-x. (d) Schematic representations of the mechanism of *in-situ* formation of high-dispersed high valence Cu species.

formed highly dispersed Cu(II) species present around the Cu NPs in the PIL layer, creating abundant Cu(0)-Cu(I), Cu(0)-Cu(II), and Cu(I)-Cu(II) interfaces.

### 3.2. CORR performance of Cu@PIL@Sn-x

The CORR performance of Cu@PIL@Sn-x (x = 0.5, 1.0, 2.0) was evaluated in a homemade flow cell with KOH electrolyte solution (1 M). The galvanostatic electrolysis was conducted by feeding 100.0 vol% CO gas into the gas chamber at the constant total current density ($j_{total}$) ranging from –100 to –700 mA cm$^{-2}$ (Fig. 3 and Figs. S5 to S8). In general, high faradaic efficiencies of C$_{2+}$ products (FE$_{C2+}$ > ~70%) were obtained at a wide $j_{total}$ range (from –100 to –700 mA cm$^{-2}$) (Fig. 3a-c). By contrast, the FE$_{C2+}$ over the pristine Cu@PIL decreases continuously with the increase of $j_{total}$ (Fig. 3d, from 89.4 % at –100 mA cm$^{-2}$ to 11.8 % at –700 mA cm$^{-2}$). It demonstrates the tolerance for a high rate of CO-to-C$_{2+}$ conversion on PIL-Cu hybrids is significantly promoted by introducing the Sn salts (0.5–2.0 mol%).

Meanwhile, the formation of C$_1$ products was controlled at a very low level (FE$_{C1}$ < ~2 %) on Cu@PIL@Sn-x (x = 0.5 and 1.0). Both display an inverted volcanic plot of FE$_{H2}$ to $j_{total}$. Particularly, a FE$_{H2}$ of ~16 % was detected at –700 mA cm$^{-2}$, corresponding to the partial current densities of H$_2$ around ~110 mA cm$^{-2}$ (Fig. S5 and S6). Thus, the H$_2$ evolution reaction (HER) accounts for the major side reaction on

these two hybrids. The CORR performance over Cu@PIL@Sn-2.0 is apparently different. Not only the side HER but also the FE$_{C1}$ at $j_{total}$ ≥ –300 mA cm$^{-2}$ (3–8 %) was apparently enhanced. The major C$_1$ product is CH$_4$ (Fig. S7), resulting from the deep hydrogenation of CO. It indicates the hydrogenation over Cu@PIL@Sn-2.0 becomes more competitive at high reaction rates. The pristine Cu@PIL behaves similarly despite the different FE values. As a result, both FE$_{H2}$ and FE$_{CH4}$ increase at higher reaction rates (Fig. S8).

The highest FE$_{C2+}$ of 96.8 % was obtained at the $j_{total}$ of –500 mA cm$^{-2}$ on Cu@PIL@Sn-1.0, delivering a high $j_{C2+}$ of –484.0 mA cm$^{-2}$. In comparison, the optimum FE$_{C2+}$ on Cu@PIL@Sn-0.5 and Cu@PIL@PIL-2.0 is 89.7% (at the $j_{total}$ of –500.0 mA cm$^{-2}$) and 94.3 % (at the $j_{total}$ of –200.0 mA cm$^{-2}$), respectively. Further, the obtained C$_{2+}$ products mainly contain acetic acid and ethanol, while bearing less ethylene (Figs. S5 to S7). Meanwhile, the highest $j_{C2+}$ of –550.2 mA cm$^{-2}$ was obtained at the $j_{total}$ of –700 mA cm$^{-2}$ on Cu@PIL@Sn-1.0, providing a moderate FE$_{C2+}$ of 78.6 %. Such a high $j_{C2+}$ outperforms most of the reported $j_{C2+}$ values obtained in flow cells (Fig. 3e and Table S11). Remarkably, the highest FE$_{C2+}$ (96.8 %) at the $j_{total}$ of –500 mA cm$^{-2}$ surpasses all the reported data of CORR conducted in the flow cell from 2018 to 2023. For instance, the pristine Cu@PIL possesses a high FE$_{C2+}$ of 95.2 % at the $j_{total}$ of only –126.2 mA cm$^{-2}$ [22]. In addition, Cu@PIL@Sn-x hybrids exhibit a significantly different performance from the documentary Cu-Sn
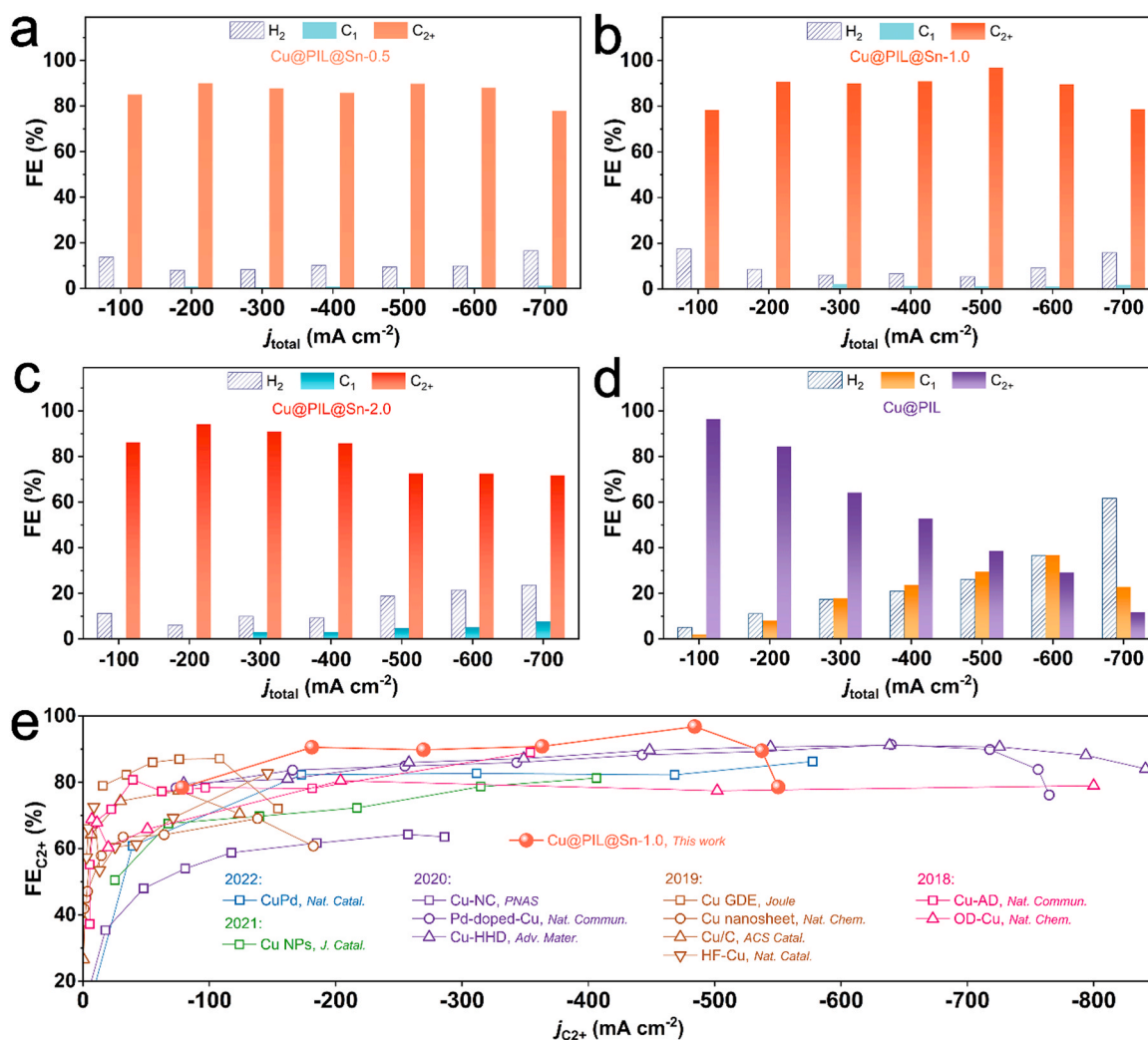


**Fig. 3.** (a-c) Faradaic efficiency (FE) of H$_2$, C$_1$ products, and C$_{2+}$ products during CORR over Cu@PIL@Sn-x at different current densities ($j_{total}$) ranging from –100 to –700 mA cm$^{-2}$. (d) FE of H$_2$, C$_1$ products, and C$_{2+}$ products during CORR over Cu@PIL at different $j_{total}$ ranging from –100 to –700 mA cm$^{-2}$. (e) Comparison of the reported electrocatalytic CO-to-C$_{2+}$ performance on flow cells from 2018 to 2023 (X-axis: $j_{C2+}$, Y-axis: FE$_{C2+}$).

bimetallic catalysts. Most of these Cu-Sn catalysts exhibit high selectivity toward $C_1$ products during the electrocatalytic $CO_2RR$ process [40–44], and only three cases selectively provide $C_{2+}$ products [45–47]. Furthermore, compared to pristine Cu@PIL, Cu@PIL@Sn-x show higher ethanol selectivity with lower $C_2H_4$ selectivity (Figs. S5 to S8). It should be attributed to the higher surface oxophilicity by introducing Sn to Cu [47], which could enhance the generation of ethanol.
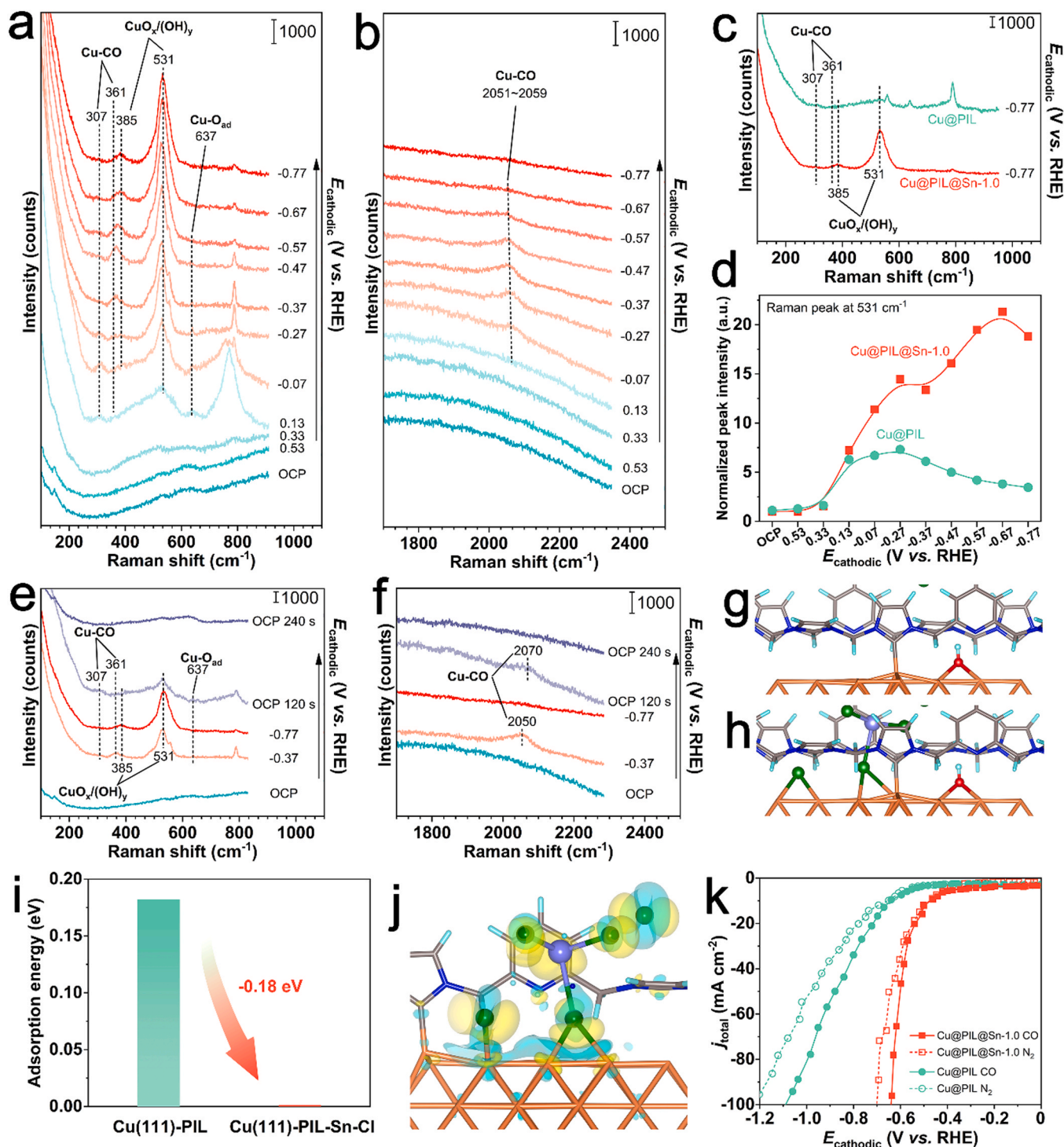


**Fig. 4.** (a-b) *In-situ* Raman spectra during CORR over Cu@PIL@Sn-1.0 in the Raman shift range of 150–900 $cm^{-1}$ and 1700–2300 $cm^{-1}$ at different $E_{cathodic}$. (c) *In-situ* Raman spectra during CORR over Cu@PIL@Sn-1.0 and Cu@PIL in the Raman shift range of 150–900 $cm^{-1}$ at −0.77 V. (d) The normalized intensity of Raman peak at 531 $cm^{-1}$ (taking the intensity at OCP as the unit) during CORR over Cu@PIL@Sn-1.0 and Cu@PIL at different $E_{cathodic}$. (e-f) *In-situ* Raman spectra over Cu@PIL@Sn-1.0 in the Raman shift range of 150–900 $cm^{-1}$ and 1700–2300 $cm^{-1}$ with and without the $E_{cathodic}$ is applied. (g-i) Optimized structures and calculated adsorption energy of *OH on Cu(111)-PIL and Cu(111)-PIL-Sn-Cl interfaces (front view; light blue: H, gray: C, blue: N, red: O, green: Cl, violet: Sn). (j) The electron density differences of Cu(111)-PIL-Sn-Cl interface (front view; the cyan and yellow regions represent electron density depletion and accumulation, respectively; the isosurface value is 0.002 e Bohr$^{-3}$) (k) Linear sweep voltammetry (LSV) curves fed with CO and $N_2$ on Cu@PIL@Sn-1.0 and Cu@PIL. (The data of Cu@PIL in (c) and (d) is reused from our previously published work, with the permission of Elsevier).

### 3.3. Mechanistic studies on the CORR process

To clarify the microenvironment of Cu sites as well as the key intermediates during the CORR, *in-situ* Raman analysis was performed over Cu@PIL@Sn-1.0. As shown in Fig. 4a, the weak and broad peaks from 500 to 650 cm$^{-1}$ at the open circuit potential (OCP) to 0.33 V were assigned to the surficial Cu$_2$O at Cu NPs [48]. Compared with the Raman response over the pristine Cu@PIL (Fig. S9) [22], Cu@PIL@Sn-1.0 possesses the weaker intensity of the independent Cu-O peaks (620–632 cm$^{-1}$) but stronger peaks for a mixture of Cu oxide and hydroxide species (*i.e.*, CuO$_x$/(OH)$_y$, 517–533 cm$^{-1}$) [48]. It signifies a higher concentration of hydroxyl functionality on Cu@PIL@Sn-1.0 than that on Cu@PIL before CORR.

Once the $E_{cathodic}$ negatively shifts to 0.13 V, the intensity of CuO$_x$/(OH)$_y$ peak increases rapidly with the appearance of a weak peak at ~385 cm$^{-1}$. These peaks were maintained at quite negative $E_{cathodic}$ of −0.77 V, which is in principle enough to support the reduction potential of Cu(OH)$_2$ to Cu$_2$O (~0.5 V) and that of Cu$_2$O to Cu(0) (~0.2 V) [48]. It suggests the formation of very rich mixed surficial CuO$_x$ and Cu(OH)$_y$ species during the CORR [48]. The feature of solely adsorbed O atoms (*O) on the Cu surface at 637 cm$^{-1}$ [48] appears at the $E_{cathodic}$ more negative than −0.57 V but the intensity is quite weak. Two peaks at 307 and 361 cm$^{-1}$ were attributed to the rotation mode of adsorbed CO (*CO) molecule and the Cu-C stretching of Cu-CO [48], respectively. These peaks appeared at the $E_{cathodic}$ lower than 0.13 V but gradually decayed at higher overpotentials than −0.37 V, signifying the fast transformation of *CO at high reaction rates. Meanwhile, the peak at 2051–2059 cm$^{-1}$ (Fig. 4b) was identified for the stretching vibration mode of the *CO [7,48]. This peak disappeared at the $E_{cathodic}$ more negative than −0.57 V (Fig. S11), confirming the fast consumption of *CO at high reaction rates. Notably, the same peak on the pristine Cu@PIL is much stronger than that on Cu@PIL@Sn-1.0 at the negative $E_{cathodic}$ (*e.g.*, −0.77 V, Fig. S10). In addition, high coverage of *CO on the surface of Cu@PIL was clearly demonstrated by the strong response at different $E_{cathodic}$ (Fig. S11) [22]. These results signify the supply rate of CO is far greater than the consumption rate of *CO on the pristine Cu@PIL. In this regard, the transformation rate of *CO is significantly enhanced on Cu@PIL@Sn-1.0, especially at high reaction rates.

Based on the literature, the high coverage of absorbed OH (*OH) on the Cu surface could promote both the hydrogenation of *CO leading to *CHO intermediates and the subsequent *CO–*CHO coupling for the generation of C$_{2+}$ products [18], while the presence of *O is also beneficial to the hydrogenation of *CO [19]. In this regard, the excellent selectivity of C$_{2+}$ products on Cu@PIL@Sn-1.0 could be attributed to the rich CuO$_x$/(OH)$_y$ species at the surface. Evidently, the peak of CuO$_x$/(OH)$_y$ on Cu@PIL@Sn-1.0 at −0.77 V is much more intense than that on pristine Cu@PIL at the same $E_{cathodic}$ (Fig. 4c). To make a clear demonstration, the intensity of the peak at 531 cm$^{-1}$ is normalized, taking the intensity at OCP as the unit, at different $E_{cathodic}$ on both the Cu@PIL@Sn-1.0 and the pristine Cu@PIL (Fig. 4d). It shows that the normalized peak intensity on Cu@PIL@Sn-1.0 increases continuously by negatively shifting the $E_{cathodic}$ from 0.33 V, which decreases after reaching the maximum value of 21.3 at −0.67 V. By comparison, the normalized peak intensity on the pristine Cu@PIL also displays a volcanic relation to the $E_{cathodic}$, but reaches the maximum value of 6.7 at −0.27 V.

The Raman analysis after removing the potential was also performed. Apparently, the intensity of the peaks assigned to CuO$_x$/(OH)$_y$ (at 531 cm$^{-1}$ and 385 cm$^{-1}$) decreases after the $E_{cathodic}$ was removed for 120 s (Fig. 4e), suggesting the mixed surficial CuO$_x$ and Cu(OH)$_y$ are produced during the electrolytic process. By contrast, the feature peaks of *CO at 307 cm$^{-1}$, 361 cm$^{-1}$, and 2070 cm$^{-1}$ arise (Fig. 4 f). It's attributed to the instantaneous accumulation of *CO intermediate by terminating both hydrogenation of *CO and the subsequent C–C coupling. The *CO-related peaks completely disappear after another 120 s, returning the original Raman characteristics of Cu@PIL@Sn-1.0

at OCP.

The density functional theory (DFT) calculations were conducted to clarify the influence of Sn species on the local enrichment of *OH during CORR. Herein, the metallic Cu-PIL interface (denoted as Cu(111)-PIL) was constructed since the applied potential during CORR is more negative than the reduction potential of high valence Cu species to metallic Cu. In addition, the Sn-Cl species were considered because the SnCl$_2$ feedstock and Cl-based PIL layer jointly ensure the presence of Cl$^-$ ions and Sn$^{\delta+}$ ions at the Cu surface during electrolysis. As a result, the *OH could be identified on the Cu(111)-PIL interface in the form of coordination to four Cu atoms with adsorption energy ($E_{ads}$) of 0.18 eV (Fig. 4 g and i, and Fig. S12). To our surprise, the $E_{ad}$ of *OH decreases to ~0 eV after introducing Sn-Cl species (*i.e.*, one Sn atom and four Cl atoms) to the Cu(111)-PIL interface (denoted as Cu(111)-PIL-Sn-Cl; Fig. 4 h and i). It highlights the positive role of Sn species on the enrichment of *OH at the surface. Further, the electron density differences analysis (Fig. 4j and Fig. S13) confirms the charge transfer from Cu atoms at the surface to both the adsorbed Cl atom and adsorbed Sn-Cl species. Besides, the Bader charge analysis (Fig. S14) indicates the surficial Cu atoms are positively charged, which is conducive to the adsorption of hydroxyl at nearby sites *via* the charge redistribution inside the metallic Cu. The influence of a single Sn atom was also examined (Fig. S15). However, the results demonstrate the presence of the Sn atom at the interface has a negative effect on the adsorption of *OH. It suggests the introduction of Sn-salts to Cu species rather than the fabrication of Cu-Sn alloy benefits the local enrichment of *OH, thereby promoting the selectivity to C$_{2+}$ products at high reaction rates.

The linear sweep voltammetry (LSV) curves on Cu@PIL and Cu@PIL@Sn-1.0 by feeding CO and N$_2$ gas, respectively, were next studied (Fig. 4k). Apparently, both LSV curves on Cu@PIL@Sn-1.0 positively shift as compared to those on the pristine Cu@PIL. It signifies not only the CORR activity but also the HER activity is enhanced by introducing the Sn-salts. For comparison, the LSV analysis was also conducted for PIL@Sn (Fig. S16). However, a very poor CORR activity was obtained, suggesting the Cu-domains in Cu@PIL@Sn-1.0 account for the active sites of CORR. In this regard, the poor performance of Cu@PIL@Sn-2.0 (Fig. 3c) could be imposed by the more competitive HER by introducing excessive Sn.

### 3.4. CORR performance with diluted CO gas and the catalytic durability

The electrocatalytic CORR performance of Cu@PIL@Sn-1.0 was also examined by feeding a diluted CO with N$_2$ of different occupations by volume (100.0–1.5 vol%). Herein, the current density of −250.0 mA cm$^{-2}$ was applied (Fig. 5a and Fig. S17), which is twice as high as that on Cu@PIL in our previous study [22]. Remarkably, an over 90% of FE$_{C2+}$ was maintained by decreasing the concentration of CO from 100.0 vol% to 40.0 vol%. Such a performance is close to that on Cu@PIL at the halved reaction rate (at −125.0 mA cm$^{-2}$) [22]. However, the FE$_{C2+}$ apparently decreases with further diluting the CO feedstock. For instance, the FE$_{C2+}$ at 20.0 vol%, 10.0 vol%, 5.0 vol%, and 1.5 vol% are 68.8 %, 51.1 %, 31.2 %, and 15.3 %, respectively. Meanwhile, a considerable amount of CH$_4$ was obtained as the only C$_1$ product under such conditions (Fig. 5a and Fig. S18), suggesting the deep hydrogenation of *CO becomes preferred due to the insufficient supply of CO. It's worthy to note that the introduction of Sn salts to Cu@PIL benefits the activity of not only the desired CORR but also the side HER (Fig. 4k). In this regard, the selectivity of C$_{2+}$ products on Cu@PIL@Sn-1.0 by feeding very low concentrations of CO at high reaction rates (*e.g.*, at −250.0 mA cm$^{-2}$) will be negatively influenced due to the strong competition of hydrogenation of intermediates or HER.

Collectively, a high $j_{C2+}$ of larger than −225 mA cm$^{-2}$ was reached on Cu@PIL@Sn-1.0 by feeding 40.0–100.0 vol% CO gas, which is twice that on Cu@PIL [22]. The definition of a metric of the minimum CO required to maintain 75% initial C$_{2+}$ selectivity (MC75$_{CO}$) [22] was employed to clarify the performance of Cu@PIL@Sn-1.0 in terms of the

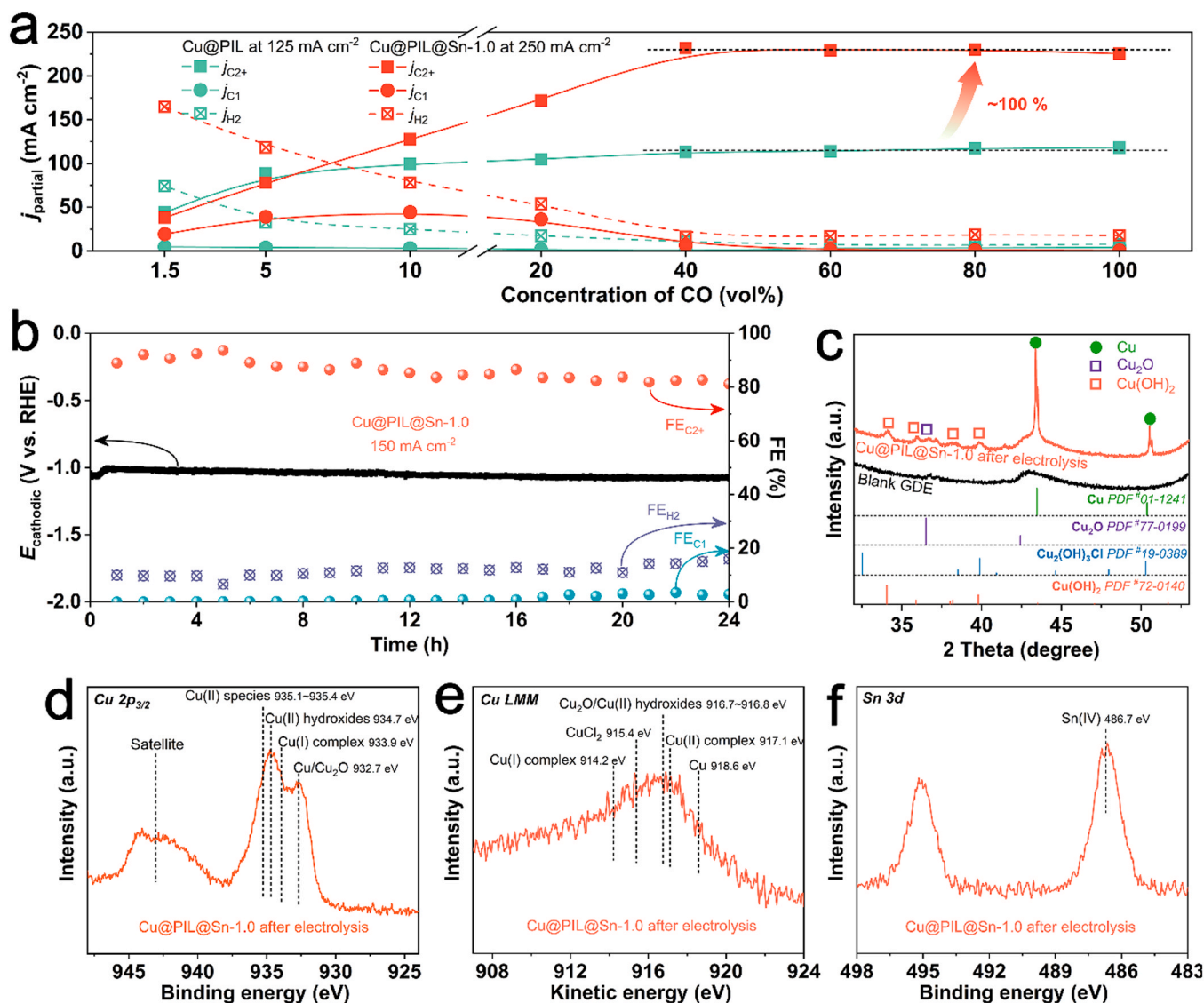**Fig. 5.** (a-b) The $j_{C2+}$, $j_{C1}$, and $j_{H2}$ during CORR over Cu@PIL@Sn-1.0 at −250.0 mA cm⁻² and Cu@PIL at −125.0 mA cm⁻² with different concentrations of CO gas. (b) Long-term stability test of Cu@PIL@Sn-1.0 at −150.0 mA cm⁻² for 24 h. (c-f) XRD pattern, XPS spectrum in Cu 2p$_{3/2}$ region, Augar spectrum in Cu LMM region, XPS spectrum in Sn 3d region of Cu@PIL@Sn-1.0 after the electrolysis. (The data of Cu@PIL in (a) is reused from our previously published work, with the permission of Elsevier).

tolerance for low-concentration CO. As a result, the MC75$_{CO}$ of Cu@PIL@Sn-1.0 at −250.0 mA cm⁻² is as low as 20.0 vol%. With feeding 5.0–20.0 vol% of CO gas, the main by-product of CH$_4$ also comes from CO electrolysis despite the decreased FE$_{C2+}$. As a whole, Cu@PIL@Sn-1.0 exhibits high capability on electrocatalytic CO conversion even with very low concentrations of CO gas.

The long-term stability of Cu@PIL@Sn-1.0 was finally tested by performing the electrolysis at −150.0 mA cm⁻² for 24 h (Fig. 5b). Evidently, the FE$_{C2+}$ of ~90% slightly decreases to ~82 % during the long-term electrolysis. Besides, the $E_{cathodic}$ negatively shifts from −1.00 V to −1.07 V after the 24-h continuous electrolysis, suggesting the stable gas-liquid pressure balance near the catalyst on the GDE. These results demonstrate the good durability of Cu@PIL@Sn-1.0 for CORR. It suggested that Cu@PIL@Sn-1.0 catalyst exhibits stable high performance under both the high reaction rate and long-term electrolysis conditions. There are three reasons. First, the introduced Sn-Cl species regulate the microenvironment of Cu, and promote the formation of high-valence Cu species and the maintenance under high current density. Second, Cl⁻ is reported to effectively improve the stability of Cu-based catalysts for C$_{2+}$ products [49]. Third, as a matrix with dense

chelating sites and electrostatic networks, PIL is conducive to maintaining the microenvironment of Cu, and provides protection for internal Cu sites [50].

The spent Cu@PIL@Sn-1.0 was characterized by XRD and XPS to clarify the variation after the electrolysis of CO. Noteworthily, the intensity of Cu species related XRD patterns decreases mainly due to the presence of the strong background signal of the GDE substrate (Fig. 5c). Besides, the metallic Cu species are dominated as demonstrated by the intense peaks marked with green circles, while the patterns for Cu$_2$O (marked with purple boxes) could also be unambiguously identified. Further, it bears the strong peaks assigned to Cu(OH)$_2$ (marked with orange boxes) but no diffraction feature for Cu$_2$(OH)$_3$Cl. The combination of the XPS spectrum in the Cu 2p$_{3/2}$ region (Fig. 5d) and the Auger spectrum in the Cu LMM region (Fig. 5e) suggests that the amount of Cu (II)-chlorides decreases. Instead, the amount of Cu(II)-hydroxides and Cu$_2$O increases, which agrees well with the *in-situ* Raman analysis (Fig. S19). These results signify the transformation from the Cu(II)-chlorides to the Cu(II)-hydroxides (*i.e.*, Cu(OH)$_x$Cl$_y$ to Cu(OH)$_2$) during the electrolysis due to the ultrahigh local concentration of OH⁻. Despite such an anion exchange, the Cl⁻ anions were well preserved in

the hybrids as demonstrated by the strong Cl XPS response (Fig. S20). Meanwhile, the state of high-valence Sn(IV) after the electrolysis was confirmed by the Sn 3d XPS analysis (Fig. 5f). The presence of these Cl$^-$ ions and the Sn(IV)-sites jointly accounts for maintaining the high-valence state of Cu species and the high performance of CORR.

## 4. Conclusions

The conclusions section should come in this section at the end of the article, before the acknowledgments. In summary, the microenvironment regulation of Cu NPs in PIL by introducing the Sn-mediated redox cycle was investigated. The dense chelating sites, the electrostatic networks, and the porous structure of the PIL layer allow the arrival of Sn species to the pre-dispersed Cu NPs in a highly dispersed manner and thereby efficient transformation of the surface of Cu NPs to high-valence counterparts *via* Sn-mediated aerobic oxidation during the preparation. These Cu@PIL@Sn-x hybrids exhibit excellent selectivity toward C$_{2+}$ products and good durability for the electrocatalytic CORR, especially at high reaction rates. Mechanistic studies signify it's attributed to not only the rich high-valence Cu species but also the adjacent Sn-Cl species. In this regard, the employment of a Cl-rich PIL layer and the Sn-based Cu-Sn bimetallic form (rather than the alloy) is essential to approach such a CORR system of high activity, high C$_{2+}$ selectivity, and high stability. These findings highlight the advantages and great potential of PIL-metal hybrids in regulating the electronic structure and microenvironment of active sites and thus improving electrocatalytic performance. In terms of practical applications, CORR is conducive to converting simple C$_1$ blocks into other diverse and high-value basic chemicals under mild conditions. In addition, CORR is a key step in electrocatalytic CO$_2$-to-C$_{2+}$ conversion. In this regard, efficient CORR is beneficial for converting CO$_2$ into multi carbon products through a two-step tandem strategy, namely the CO$_2$-to-CO-to-C$_{2+}$ process with high efficiency.

## CRediT authorship contribution statement

**Yi-Ran Du:** Formal analysis; Visualization; Methodology. **Xiao-Qiang Li:** Data curation; Writing – original draft. **Guo-Yi Duan:** Methodology; Data curation; Formal analysis; Visualization; Writing – original draft. **Yue Pan:** Writing – review & editing. **En-Lai Gao:** Theoretical calculation. **Bao-Hua Xu:** Conceptualization; Methodology; Writing – review & editing; Supervision; Project administration.

## Declaration of Competing Interest

The authors declare that they have no known competing financial interests or personal relationships that could have appeared to influence the work reported in this paper.

## Data availability

I have shared the link to my data.

## Acknowledgments

## Appendix A. Supporting information

Supplementary data associated with this article can be found in the online version at doi:10.1016/j.apcatb.2023.122969.

## References

[1] C. Wang, B. Liu, P. Liu, K. Huang, N. Xu, H. Guo, P. Bai, L. Ling, X. Liu, S. Mintova, Elucidation of the reaction mechanism of indirect oxidative carbonylation of methanol to dimethyl carbonate on Pd/NaY catalyst: direct identification of reaction intermediates, J. Catal. 412 (2022) 30–41, https://doi.org/10.1016/j.jcat.2022.06.002.

[2] V. Pandey, R. Singh, K.K. Pant, S. Upadhyayula, Experimental and theoretical study unveiling the role of solvents on CO activation and hydrogenation to methanol in three-phase reactor system, J. Mol. Struct. 1274 (2023), 134392, https://doi.org/10.1016/j.molstruc.2022.134392.

[3] L.U. Okonye, Y. Yao, J. Ren, X. Liu, D. Hildebrandt, A perspective on the activation energy dependence of the Fischer-Tropsch synthesis reaction mechanism, Chem. Eng. Sci. 265 (2023), 118259, https://doi.org/10.1016/j.ces.2022.118259.

[4] M. Chu, C. Chen, Y. Wu, X. Yan, S. Jia, R. Feng, H. Wu, M. He, B. Han, Enhanced CO$_2$ electroreduction to ethylene via strong metal-support interaction, Green Energy Environ. (2020) 792–798, https://doi.org/10.1016/j.gee.2020.12.001.

[5] K. Ye, T. Liu, Y. Song, Q. Wang, G. Wang, Tailoring the interactions of heterogeneous Ag$_2$S/Ag interface for efficient CO$_2$ electroreduction, Appl. Catal. B-Environ. 296 (2021), 120342, https://doi.org/10.1016/j.apcatb.2021.120342.

[6] Y. Zou, S. Wang, An investigation of active sites for electrochemical CO$_2$ reduction reactions: from in situ characterization to rational design, Adv. Sci. 8 (2021), 2003579, https://doi.org/10.1002/advs.202003579.

[7] Z.Z. Niu, F.Y. Gao, X.L. Zhang, P.P. Yang, R. Liu, L.P. Chi, Z.Z. Wu, S. Qin, X. Yu, M. R. Gao, Hierarchical copper with inherent hydrophobicity mitigates electrode flooding for high-rate CO$_2$ electroreduction to multicarbon products, J. Am. Chem. Soc. 143 (2021) 8011–8021, https://doi.org/10.1021/jacs.1c01190.

[8] M. Ma, E.L. Clark, K.T. Therkildsen, S. Dalsgaard, I. Chorkendorff, B. Seger, Insights into the carbon balance for CO$_2$ electroreduction on Cu using gas diffusion electrode reactor designs, Energy Environ. Sci. 13 (2020) 977–985, https://doi.org/10.1039/d0ee00047g.

[9] C.M. Gabardo, C.P. O'Brien, J.P. Edwards, C. McCallum, Y. Xu, C.-T. Dinh, J. Li, E. H. Sargent, D. Sinton, Continuous carbon dioxide electroreduction to concentrated multi-carbon products using a membrane electrode assembly, Joule 3 (2019) 2777–2791, https://doi.org/10.1016/j.joule.2019.07.021.

[10] J. Sisler, S. Khan, A.H. Ip, M.W. Schreiber, S.A. Jaffer, E.R. Bobicki, C.-T. Dinh, E. H. Sargent, Ethylene electrosynthesis: a comparative techno-economic analysis of alkaline vs membrane electrode assembly vs CO$_2$–CO–C$_2$H$_4$ tandems, ACS Energy Lett. 6 (2021) 997–1002, https://doi.org/10.1021/acsenergylett.0c02633.

[11] M. Jouny, G.S. Hutchings, F. Jiao, Carbon monoxide electroreduction as an emerging platform for carbon utilization, Nat. Catal. 2 (2019) 1062–1070, https://doi.org/10.1038/s41929-019-0388-2.

[12] F.P. García de Arquer, C.-T. Dinh, A. Ozden, J. Wicks, C. McCallum, A.R. Kirmani, D.-H. Nam, C. Gabardo, A. Seifitokaldani, X. Wang, Y.C. Li, F. Li, J. Edwards, L. J. Richter, S.J. Thorpe, D. Sinton, E.H. Sargent, CO$_2$ electrolysis to multicarbon products at activities greater than 1 A cm$^{-2}$, Science 367 (2020) 661–666, https://doi.org/10.1126/science.aay4217.

[13] A. Ozden, F. Li, F.P. García de Arquer, A. Rosas-Hernández, A. Thevenon, Y. Wang, S.-F. Hung, X. Wang, B. Chen, J. Li, J. Wicks, M. Luo, Z. Wang, T. Agapie, J. C. Peters, E.H. Sargent, D. Sinton, High-rate and efficient ethylene electrosynthesis using a catalyst/promoter/transport layer, ACS Energy Lett. 5 (2020) 2811–2818, https://doi.org/10.1021/acsenergylett.0c01266.

[14] W. Ma, S. Xie, T. Liu, Q. Fan, J. Ye, F. Sun, Z. Jiang, Q. Zhang, J. Cheng, Y. Wang, Electrocatalytic reduction of CO$_2$ to ethylene and ethanol through hydrogen-assisted C–C coupling over fluorine-modified copper, Nat. Catal. 3 (2020) 478–487, https://doi.org/10.1038/s41929-020-0450-0.

[15] Q. Lei, H. Zhu, K. Song, N. Wei, L. Liu, D. Zhang, J. Yin, X. Dong, K. Yao, N. Wang, X. Li, B. Davaasuren, J. Wang, Y. Han, Investigating the origin of enhanced C$_{2+}$ selectivity in oxide-/hydroxide-derived copper electrodes during CO$_2$ electroreduction, J. Am. Chem. Soc. 142 (2020) 4213–4222, https://doi.org/10.1021/jacs.9b11790.

[16] S.Y. Lee, H. Jung, N.K. Kim, H.S. Oh, B.K. Min, Y.J. Hwang, Mixed copper states in anodized Cu electrocatalyst for stable and selective ethylene production from CO$_2$ reduction, J. Am. Chem. Soc. 140 (2018) 8681–8689, https://doi.org/10.1021/jacs.8b02173.

[17] D. Zhong, Z.J. Zhao, Q. Zhao, D. Cheng, B. Liu, G. Zhang, W. Deng, H. Dong, L. Zhang, J. Li, J. Li, J. Gong, Coupling of Cu(100) and (110) facets promotes carbon dioxide conversion to hydrocarbons and alcohols, Angew. Chem. Int. Ed. 60 (2021) 4879–4885, https://doi.org/10.1002/anie.202015159.

[18] M. Sun, A. Staykov, M. Yamauchi, Understanding the roles of hydroxide in CO$_2$ electroreduction on a Cu electrode for achieving variable selectivity, ACS Catal. (2022) 14856–14863, https://doi.org/10.1021/acscatal.2c03650.

[19] M. He, X. Chang, T.-H. Chao, C. Li, W.A. Goddard, M.-J. Cheng, B. Xu, Q. Lu, Selective enhancement of methane formation in electrochemical CO$_2$ reduction enabled by a Raman-inactive oxygen-containing species on Cu, ACS Catal. (2022) 6036–6046, https://doi.org/10.1021/acscatal.2c00087.

[20] W. Zhang, X. Wen, S. Yang, Y. Berta, Z.L. Wang, Single-crystalline scroll-type nanotube arrays of copper hydroxide synthesized at room temperature, Adv. Mater. 15 (2003) 822–825, https://doi.org/10.1002/adma.200304840.

[21] C.-Y. Lin, Y.-H. Lai, D. Mersch, E. Reisner, Cu$_2$O|NiO$_x$ nanocomposite as an inexpensive photocathode in photoelectrochemical water splitting, Chem. Sci. 3 (2012) 3482, https://doi.org/10.1039/c2sc20874a.

[22] G.-Y. Duan, X.-Q. Li, J.-W. Chen, G.-R. Ding, P.-X. Guan, B.-H. Xu, Poly(ionic liquid) boosts overall performance of electrocatalytic reduction of low concentration of CO gas, Chem. Eng. J. 451 (2023), 138491, https://doi.org/10.1016/j.cej.2022.138491.

[23] X.-Q. Li, G.-Y. Duan, J.-W. Chen, L.-J. Han, S.-J. Zhang, B.-H. Xu, Regulating electrochemical $CO_2RR$ selectivity at industrial current densities by structuring copper@poly(ionic liquid) interface, Appl. Catal. B-Environ. 297 (2021) 120471, https://doi.org/10.1016/j.apcatb.2021.120471.

[24] X.-Q. Li, G.-Y. Duan, X.-X. Yang, L.-J. Han, B.-H. Xu, Electroreduction of carbon dioxide to multi-electron reduction products using poly(ionic liquid)-based Cu-Pd catalyst, Fundam. Res. 2 (2022) 937–945, https://doi.org/10.1016/j.fmre.2021.12.009.

[25] X.-Q. Li, G.-Y. Duan, R. Wang, L.-J. Han, Y.-F. Wang, B.-H. Xu, Poly(ionic liquid)-based bimetallic tandem catalysts for highly efficient carbon dioxide electroreduction, Appl. Catal. B-Environ. 313 (2022) 121459, https://doi.org/10.1016/j.apcatb.2022.121459.

[26] G.-Y. Duan, X.-Q. Li, G.-R. Ding, L.-J. Han, B.-H. Xu, S.-J. Zhang, Highly efficient electrocatalytic $CO_2$ reduction to $C_{2+}$ products on a poly(ionic liquid)-based $Cu^0$-$Cu^I$ tandem catalyst, Angew. Chem. Int. Ed. 61 (2022), e202110657, https://doi.org/10.1002/anie.202110657.

[27] J. Peng, S. Xian, J. Xiao, Y. Huang, Q. Xia, H. Wang, Z. Li, A supported Cu(I)@MIL-100(Fe) adsorbent with high CO adsorption capacity and $CO/N_2$ selectivity, Chem. Eng. J. 270 (2015) 282–289, https://doi.org/10.1016/j.cej.2015.01.126.

[28] K.F. Kusano, M. Uchikoshi, K. Mimura, M. Isshiki, Low-temperature oxidation of Cu(100), Cu(110) and Cu(111), Oxid. Met. 82 (2014) 181–193, https://doi.org/10.1007/s11085-014-9486-3.

[29] M. Thommes, Physisorption of gases, with special reference to the evaluation of surface area and pore size distribution (IUPAC Technical Report), Chem. Int. 38 (2016), https://doi.org/10.1515/ci-2016-0119.

[30] D.P. Drolet, D.M. Manuta, A.J. Lees, A.D. Katnani, G.J. Coyle, FT-IR and XPS study of copper(II) complexes of imidazole and benzimidazole, Inorg. Chim. Acta 146 (1988) 173–180, https://doi.org/10.1016/s0020-1693(00)80605-2.

[31] S.P. Roe, J.O. Hill, J. Liesegang, An X-ray photoelectron spectroscopic study of some bis(diamine)-copper (II) complexes, J. Electron. Spectrosc. Relat. Phenom. 46 (1988) 315–324, https://doi.org/10.1016/0368-2048(88)85029-1.

[32] R.P. Vasquez, $CuCl_2$ by XPS, Surf. Sci. Spectra 2 (1993) 160–164, https://doi.org/10.1116/1.1247736.

[33] G. Deroubaix, P. Marcus, X-ray photoelectron spectroscopy analysis of copper and zinc oxides and sulphides, Surf. Interface Anal. 18 (1992) 39–46, https://doi.org/10.1002/sia.740180107.

[34] J.G. Jolley, G.G. Geesey, M.R. Hankins, R.B. Wright, P.L. Wichlacz, Auger electron and X-ray photoelectron spectroscopic study of the biocorrosion of copper by alginic acid polysaccharide, Appl. Surf. Sci. 37 (1989) 469–480, https://doi.org/10.1016/0169-4332(89)90505-9.

[35] A.C. Miller, G.W. Simmons, Copper by XPS, Surf. Sci. Spectra 2 (1993) 55–60, https://doi.org/10.1116/1.1247725.

[36] M. Andersson, J. Blomquist, B. Folkesson, R. Larsson, P. Sundberg, Esca, mössbauer and infrared spectroscopic investigations of a series of tin complexes, J. Electron. Spectrosc. Relat. Phenom. 40 (1986) 385–396, https://doi.org/10.1016/0368-2048(86)80047-0.

[37] J.C.C. Fan, J.B. Goodenough, X-ray photoemission spectroscopy studies of Sn-doped indium-oxide films, J. Appl. Phys. 48 (1977) 3524–3531, https://doi.org/10.1063/1.324149.

[38] A.A. Bakke, H.-W. Chen, W.L. Jolly, A table of absolute core-electron binding-energies for gaseous atoms and molecules, J. Electron. Spectrosc. Relat. Phenom. 20 (1980) 333–366, https://doi.org/10.1016/0368-2048(80)85030-4.

[39] S.C. Avanzino, W.L. Jolly, An X-ray photoelectron spectroscopy study of volatile tin compounds, J. Electron. Spectrosc. Relat. Phenom. 8 (1976) 15–22, https://doi.org/10.1016/0368-2048(76)80002-3.

[40] D. Li, L. Huang, Y. Tian, T. Liu, L. Zhen, Y. Feng, Facile synthesis of porous Cu-Sn alloy electrode with prior selectivity of formate in a wide potential range for $CO_2$ electrochemical reduction, Appl. Catal. B-Environ. 292 (2021) 120119, https://doi.org/10.1016/j.apcatb.2021.120119.

[41] K. Ye, Z. Zhou, J. Shao, L. Lin, D. Gao, N. Ta, R. Si, G. Wang, X. Bao, In situ reconstruction of a hierarchical Sn-Cu/$SnO_x$ core/shell catalyst for high-performance $CO_2$ electroreduction, Angew. Chem. Int. Ed. 59 (2020) 4814–4821, https://doi.org/10.1002/anie.201916538.

[42] W. Wang, Z. Wang, R. Yang, J. Duan, Y. Liu, A. Nie, H. Li, B.Y. Xia, T. Zhai, In situ phase separation into coupled interfaces for promoting $CO_2$ electroreduction to formate over a wide potential window, Angew. Chem. Int. Ed. 60 (2021) 22940–22947, https://doi.org/10.1002/anie.202110000.

[43] X. Zhong, S. Liang, T. Yang, G. Zeng, Z. Zhong, H. Deng, L. Zhang, X. Sun, Sn dopants with synergistic oxygen vacancies boost $CO_2$ electroreduction on CuO nanosheets to CO at low overpotential, ACS Nano 16 (2022) 19210–19219, https://doi.org/10.1021/acsnano.2c08436.

[44] M. Zhang, Z. Zhang, Z. Zhao, H. Huang, D.H. Anjum, D. Wang, J.-H. He, K.-W. Huang, Tunable selectivity for electrochemical $CO_2$ reduction by bimetallic Cu–Sn catalysts: elucidating the roles of Cu and Sn, ACS Catal. 11 (2021) 11103–11108, https://doi.org/10.1021/acscatal.1c02556.

[45] X. Chen, D.A. Henckel, U.O. Nwabara, Y. Li, A.I. Frenkel, T.T. Fister, P.J.A. Kenis, A.A. Gewirth, Controlling speciation during $CO_2$ reduction on Cu-alloy electrodes, ACS Catal. 10 (2019) 672–682, https://doi.org/10.1021/acscatal.9b04368.

[46] L. Shang, X. Lv, L. Zhong, S. Li, G. Zheng, Efficient $CO_2$ electroreduction to ethanol by $Cu_3Sn$ catalyst, Small Methods 6 (2022), e2101334, https://doi.org/10.1002/smtd.202101334.

[47] M. Li, N. Song, W. Luo, J. Chen, W. Jiang, J. Yang, Engineering surface oxophilicity of copper for electrochemical $CO_2$ reduction to ethanol, Adv. Sci. 10 (2023), e2204579, https://doi.org/10.1002/advs.202204579.

[48] Y. Zhao, X. Chang, A.S. Malkani, X. Yang, L. Thompson, F. Jiao, B. Xu, Speciation of Cu surfaces during the electrochemical CO reduction reaction, J. Am. Chem. Soc. 142 (2020) 9735–9743, https://doi.org/10.1021/jacs.0c02354.

[49] M. Li, Y. Ma, J. Chen, R. Lawrence, W. Luo, M. Sacchi, W. Jiang, J. Yang, Residual chlorine induced cationic active species on a porous copper electrocatalyst for highly stable electrochemical $CO_2$ reduction to $C_2$, Angew. Chem. Int. Ed. 60 (2021) 11487–11493, https://doi.org/10.1002/anie.202102606.

[50] H. Zhang, C. Wang, H. Luo, J. Chen, M. Kuang, J. Yang, Iron nanoparticles protected by chainmail-structured graphene for durable electrocatalytic nitrate reduction to nitrogen, Angew. Chem. Int. Ed. 62 (2023), e202217071, https://doi.org/10.1002/anie.202217071.